



Contents lists available at ScienceDirect

## Mechanical Systems and Signal Processing

journal homepage: [www.elsevier.com/locate/ymssp](http://www.elsevier.com/locate/ymssp)

## A framework for the damage evaluation of acoustic emission signals through Hilbert–Huang transform

Giulio Siracusano<sup>a,\*</sup>, Francesco Lamonaca<sup>b,c</sup>, Riccardo Tomasello<sup>b</sup>,  
 Francesca Garescì<sup>d</sup>, Aurelio La Corte<sup>e</sup>, Domenico Luca Carnì<sup>b</sup>,  
 Mario Carpentieri<sup>f</sup>, Domenico Grimaldi<sup>b</sup>, Giovanni Finocchio<sup>a</sup>

<sup>a</sup> Department of Mathematical and Computer Sciences, Physical Sciences and Earth Sciences, University of Messina,  
 Viale F. Stagno d'Alcontres, 31-98166 Messina, Italy

<sup>b</sup> Department of Informatics, Modeling, Electronics and System Engineering, University of Calabria, 87036 Rende, CS, Italy

<sup>c</sup> Department of Engineering, University of Sannio, 82100 Benevento, Italy

<sup>d</sup> Department of Engineering, University of Messina, C. di Dio, S. Agata, 98166 Messina, Italy

<sup>e</sup> Department of Electric, Electronic and computer Engineering, University of Catania, Viale Andrea Doria 6, 95125 Catania, Italy

<sup>f</sup> Department of Electrical and Information Engineering, Politecnico di Bari, via E. Orabona 4, 70125 Bari, Italy

## ARTICLE INFO

## Article history:

Received 3 August 2015

Received in revised form

2 December 2015

Accepted 9 December 2015

## Keywords:

Acoustic emission

Damage detection

Structural Health Monitoring

Compression test

Hilbert–Huang Transform

3D crack localization

## ABSTRACT

The acoustic emission (AE) is a powerful and potential nondestructive testing method for structural monitoring in civil engineering. Here, we show how systematic investigation of crack phenomena based on AE data can be significantly improved by the use of advanced signal processing techniques. Such data are a fundamental source of information that can be used as the basis for evaluating the status of the material, thereby paving the way for a new frontier of innovation made by data-enabled analytics. In this article, we propose a framework based on the Hilbert–Huang Transform for the evaluation of material damages that (i) facilitates the systematic employment of both established and promising analysis criteria, and (ii) provides unsupervised tools to achieve an accurate classification of the fracture type, the discrimination between longitudinal ( $P$ -) and traversal ( $S$ -) waves related to an AE event. The experimental validation shows promising results for a reliable assessment of the health status through the monitoring of civil infrastructures.

© 2015 Elsevier Ltd. All rights reserved.

## 1. Introduction

The behavior of heterogeneous materials, such as concrete, under compression load is a complex process involving different phenomena and it is governed by the nucleation and the growth of defects and damages. As the number of defects increases, a non-linear response related to a change of the mechanical parameters (e.g. nominal strength), and eventually irreversible processes leading to material collapse take place [1]. The failure mechanism is strongly dependent on different aspects, the evolution of the cracking patterns during the loading process, the shape and size of the specimens, and the type of applied stress [2].

Due to the release of localized internal energy, acoustic emission (AE) data [3] have been widely used for Structural Health Monitoring (SHM) [4–8] and adopted as a mean of identifying defects in pipelines [9] and composite materials [10].

\* Corresponding author.

E-mail address: [giuliosiracusano@gmail.com](mailto:giuliosiracusano@gmail.com) (G. Siracusano).

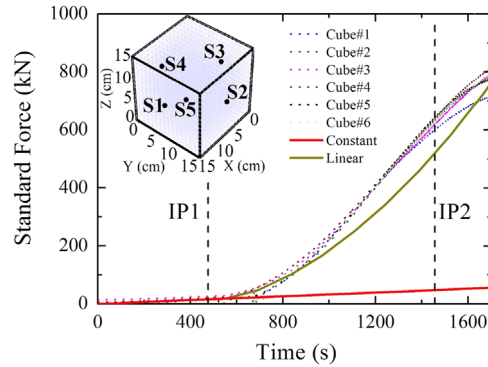


**Fig. 1.** Experimental load-vs-time diagrams (dotted lines) for the samples under test, and simulation results considering either constant (red line) and time-varying Young modulus for the specimen (gold line). Inset: position of the piezoelectric transducers for testing purposes. (For interpretation of the references to color in this figure legend, the reader is referred to the web version of this article.)

This approach is beneficial to characterize the cracks, enabling an early assessment of both material condition [11] and possible large-scale failure. Such monitoring method helps to manage the structures safely and economically. The analysis of AE data has significant advantages as compared to other nondestructive testing (NDT) techniques, such as ultrasound [12] and x-rays [13,14]. The key one is that the development of cracks can be studied on site directly and the retrieved information can be used to reveal the existence of different types of deformation [15].

From an experimental point of view, the AE signals related to the elastic waves resulting from damage events are recorded by piezoelectric transducers, which are commonly placed on the outer surfaces of the specimen [16], which convert the elastic waves to electrical signals. However, recent findings [17] have pointed out how disturbances (e.g. scattering attenuation due to damage accumulation, viscous damping, inhomogeneity of concrete, internal sample structure defects, etc.) can give rise to misleading data if they are not well accounted and minimized [18]. In order to avoid that, suitable computing environments including superior denoising performance and accurate algorithms for the efficient estimation of AE parameters have to be realized and tested [19].

Here, we have developed a processing framework to provide advanced analysis tools required to build the next-generation of SHM systems. It comprises an algorithm to perform sensor transfer function removal (TFR) adjusting the influence of the acquisition system, and an unsupervised tool based on the Hilbert–Huang Transform (HHT) [20,21] that enhances the Signal to Noise Ratio (SNR) [22] and permits both a better quantification [23–25] of AE parameters (for example the estimation of the propagating speed) and the damage location by using the Multilateration (MLT) algorithm [26]. The proposed tool is tested on experimental data measured by a multi-sensor Acquisition System (AS) [27].

The paper is organized as follows. Section 2 provides information about the acquisition system and the experimental setup. Section 3 describes the proposed framework. Sections 4 and 5 present results and discussions. Finally, in Section 6 the conclusions are provided.

## 2. Experimental setup

The AE measurements have pointed out that elastic energy due to a crack formation is characterized by modes with frequency in preferential bands [28] that, for cementitious materials, are in the range of kHz [16]. In concrete, for the characterization of AE data, standardization is currently being attempted [29], meaning to propose a well established type of sensors and measurement procedures. With this regards, we have already developed a multi-triggered acquisition system that takes into account emerging standards and enables both high sampling frequencies and reduced storage requirements [27,30], as detailed below.

The experimental setup consists of:

- One hydraulic press with a closed loop governing system with 3000 kN and accuracy class 0.5%, connected to the AS to record the load–displacement diagram;
- Five AE transducers, R15 $\alpha$ , with a peak sensitivity of 69 V/(m/s), resonant frequency 150 kHz, and directionality  $\pm 1.5$  dB [22,31];
- The Logic Flat Amplifier Trigger generator (L-FAT) [27];
- Two Data acquisition boards (DAQ) NI-6110 with four input channels, 12 bit resolution, and sampling frequency  $f_{AS}=5$  Msample/s  $\pm 1154$  sample/s. A channel (Ch) is associated to each transducer;
- A self-implemented processing framework.

A complete description about acquisition system is provided in Ref. [27]. With respect to that configuration, the L-FAT architecture is now extended to enable the connection of five sensors. The standard of the hardware and software system are implemented as described in Ref. [16]. Experimental tests were conducted on concrete cubic samples with no steel reinforcement, having a volume  $15 \times 15 \times 15 \text{ cm}^3$ , cured 28 days at a temperature  $20 \pm 2^\circ\text{C}$  and a relative humidity equal to 95% according to EN 12390-3 [32].

The calibration of the system was carried out after the installation of the transducers. For this setup, four AE transducers were placed on the center of the four sides of the specimen (S1–S4 in the inset of Fig. 1), while an additional transducer was added on one vertical face at a distance of 2 cm from the upper right corner (S5), in order to remove degeneracies in the localization algorithm (see Section 3.6). The hydraulic press was connected to a data-acquiring device to record the load-time diagram showed in Fig. 1 for different samples. We have studied over 30 specimens. In order to make a readable figure, we represent data from six different samples (colored dotted lines). The load-time diagram exhibits two Inflection Points (IP) consistently with previous experimental data. After the second inflection point, the response becomes strongly non-linear indicating that the specimen is damaged. The region between the two IPs is the most important in terms of AE data. Fig. 1 also shows two theoretical load-vs-time diagrams [33, 34] computed with a Finite Element (FE) solver. The first one, computed for a constant Young's modulus ( $E = 3.14 \cdot 10^{10} \text{ Pa}$ ) (red line), shows a good agreement with the experimental data up to the first inflection point. In the other one (gold line), the Young's modulus is considered constant up to the IP1 ( $E = 3.14 \cdot 10^{10} \text{ Pa}$ ) and then it increases linearly as a function of the displacement,  $\gamma$ , up to IP2 (the following expression  $E(\gamma) = 3.63 \cdot 10^8 \cdot \gamma - 1.86 \cdot 10^{11} \text{ Pa}$  has been used to fit the data). At IP2, the Young modulus is  $E = 4.67 \cdot 10^{11} \text{ Pa}$  which is consistent with the value computed by considering the average slope of the load-time diagram from the IP1 to IP2.

The results we have achieved in processing the AE data are qualitatively the same for all the samples, thus in the rest of the paper we will discuss in detail only one sample. We have collected 879 triggered events from the sample Cube 1, during a time interval of 1691s. The AEs were numbered in progressive order.

Silicon grease was used as coupling agent between the sensor and the concrete surface [2]. In this experiment, TFR (see Section 3) enables to adjust the effects of the transducer also if the main original spectral components of the signal [15–50 kHz] are out of the best sensor active frequency range [50–400 kHz]. If the voltage of a sensor goes beyond the threshold [35], an event is triggered and the signals from all transducers are pre-amplified, digitized and collected by a multi-channel system with a sampling rate of 5 MHz, where each channel (Ch1–Ch5) corresponds to a single sensor (S1–S5). The software, in cooperation with the acquisition board, automatically triggers the recording of relevant AEs [36]. The threshold is *a priori* set by the operator according to the noise floor and calibration procedures as defined in EN 13477-2 [37] standard code. The collected experimental measurements are AE events generated by a controlled uniaxial compression of the specimen due to an hydraulic press pushing from the top to the bottom with a constant displacement rate of 0.1 mm/min (a feedback process permits to control the displacement by adapting the standard force [1]) until failure.

### 3. Framework for the analysis of acoustic emission data

Fig. 2 shows the schematic block diagram of the framework for the processing of AE data. From a given signal, each block on the chain performs different I/O operations and it is numbered depending on whether it is used to provide preparatory (sequential) or complementary (parallel) computations. The role of each computational block is summarized below: a raw transducer measurement,  $r(t)$ , is deconvoluted [16] in (I) with the resonant sensor transfer function generating a reconstructed signal,  $s(t)$ . Then, such signal is further processed in (II) by means of the HHT that provides two outputs: (a) a denoised signal,  $\hat{s}(t)$ , and (b) a finite set of  $N$  intrinsic mode functions (IMF),  $y_i$  ( $i = 1 \dots N$ ). These outputs are used as inputs of the blocks (III.1–4) in order to perform the operations reported below.

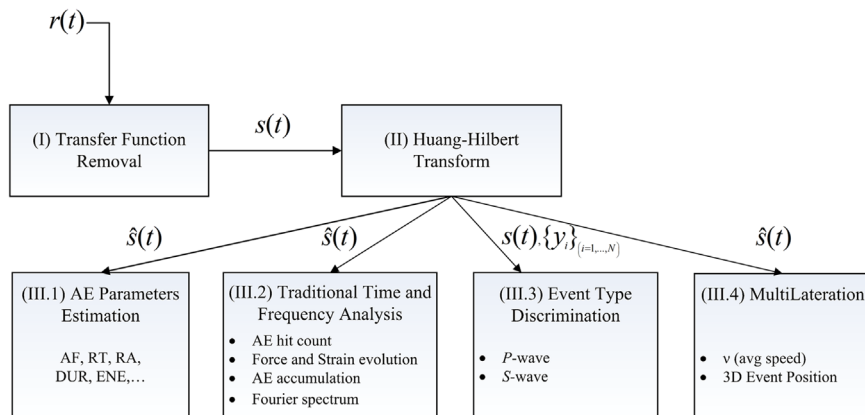


Fig. 2. Simplified block diagram of our processing framework.

(III.1) To compute the most representative AE parameters, such as the average frequency (AF), the rise time (RT), the duration (DUR) and rise angle (RA), the peak amplitude, the energy (ENE) from  $\widehat{s}(t)$ . To correlate the AE parameters with damage processes and failure modes. Specific AE indexes have been used to identify the achievement of critical failures [38] in advance if compared to traditional visual observation or drop of mechanical load readings;

(III.2) To monitor hit counts and to analyze temporal (e.g. accumulation of AE events as a function of time) and spectral information from failure events (e.g. variation of average central frequency and amplitude during test);

(III.3) To enable unambiguous discrimination between longitudinal waves (*P*-waves) and traversal waves (*S*-waves) from IMFs providing unsupervised classification of the damage events;

(III.4) To extend a MLT technique in order to provide the joint estimation of pulse average propagating speed and spatial localization of the AE sources from the measurement of Time Difference of Arrival (TDOA) of signals recorded by an array of sensors. AE localization technology can reflect the damage process more intuitively than the parameter analysis methods.

### 3.1. Transfer function removal

The first block of the processing tool implements a TFR algorithm to perform the deconvolution of the measured signals, from the sensor and amplifier transfer function [7]. This is necessary in order to minimize the presence of artifacts in the measurements caused mainly by the acquisition system. From a mathematical point of view, detection, recording and amplification can be modeled with different transfer functions  $w(t)$ , thus an AE signal  $r(t)$  is given by a convolution product [16]:

$$r(t) = w_f(t) \otimes w_a(t) \otimes w_s(t) \otimes s(t) \quad (1)$$

where  $s(t)$  is the signal emitted after the crack once it reaches the transducer,  $w_s(t)$  is the sensor transfer function,  $w_f(t)$  and  $w_a(t)$  are the transfer functions of the filter and the amplifier, respectively. In the frequency domain, Eq. (1) holds:

$$R(f) = W_f(f) \cdot W_a(f) \cdot W_s(f) \cdot S(f) \quad (2)$$

If the filter  $W_f(f)$  and the amplifier  $W_a(f)$  are well designed, their frequency response in the spectral region of the AE signal are almost flat and can be safely neglected:

$$R(f) \approx W_s(f) \cdot S(f) \quad (3)$$

then  $S(f) \approx \frac{R(f)}{W_s(f)}$ . In our case, the approximation in Eq. (3) can be considered valid.

Here, the frequency response of the resonant transducer is expected to significantly affect the spectral components of recorded AE signals, by introducing a selective amplification of a given range of frequencies. The results of TFR show that the method successfully recovers the solicitation that was previously altered by the sensor frequency response and whose output can be considered similar to the waveforms if captured from flat broadband transducers [39–41]. We provide in Fig. 3 the comparison between raw sensor measurements,  $r_{k,z}(t)$  (here, the indexes  $k$  and  $z$  represent the number of the event and the channel of the corresponding transducer, *Ch.*, respectively) and reconstructed signals  $s_{k,z}(t)$ . In Fig. 3(a), the type of AE related to the event 4 (Ch.2) is the result of a typical tensile deformation and can be intuitively identified by the shape of the reconstructed signal  $s_{4,2}(t)$  (black line), while it is hard the classification from the  $r_{4,2}(t)$  (gray line) without evaluating AE

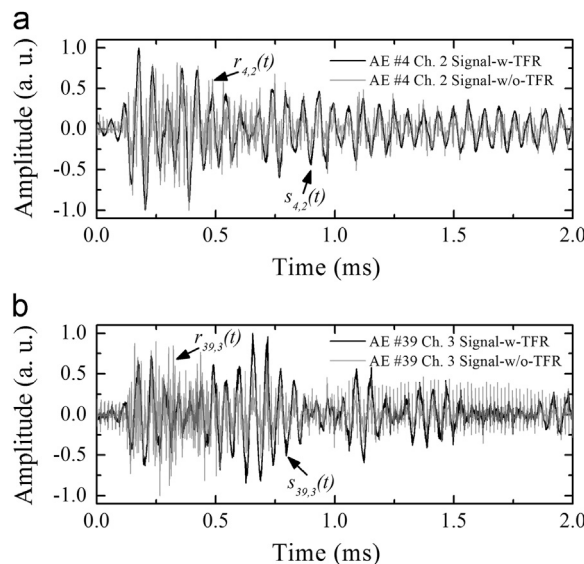


**Fig. 3.** (a) Time domain signals linked to the event 4 (Ch.2) (gray line) and after the TFR (black line). (b) Again, signals linked to the event 39 (Ch.3) (gray line) and after the TFR (black line).

parameters, at least. Again, the AE event 39 (Ch.3) displayed in Fig. 3(b) shows a common shear stress (black line), whose shape can be recognized more intuitively from  $s_{39,3}(t)$  instead of  $r_{39,3}(t)$  (gray line).

The substantial difference between captured and reconstructed signals highlights how, for an unbiased characterization of AE sources, it is crucial to know the weights of the different transfer functions associated with the acquisition system in order to correct their influences.

### 3.2. Hilbert–Huang transform

HHT is a recently developed method which has proved to be a useful tool for studying the nonstationary and nonlinear behavior of time series [6,42] with a lower computational cost as compared to Principal Component Analysis (PCA) and clusterization [43], or machine learning algorithms [44]. By means of this technique, complex sets of nonlinear and non-stationary data can be decomposed into a finite collection of individual characteristic oscillatory modes, named IMF. HHT is a combination of Hilbert Transform (HT) operator and Empirical Mode Decomposition (EMD). EMD is an adaptive and efficient method applied to decompose nonstationary and nonlinear signals.

In block (II), the reconstructed signals  $s_{k,z}(t)$  are further processed by using the HHT to produce an output with an enhanced SNR  $\hat{s}_{k,z}(t)$  (obtained by removing high-frequency noise and low frequency trend), and to get a complete signal decomposition into IMFs,  $y_i$  ( $i=1,\dots,N$ ) using EMD, so that  $s_{k,z}(t) \cong \sum y_i$ . Since accurate filtering capabilities are the key ingredient to increase the reliability in AE analysis, HHT is considered more appropriate for the full investigation of both nonstationary and nonlinear components of elastic waves than other techniques known in literature [45,46], especially for its better resolution in time and frequency domain [47].

The initial attempt at using HHT as a denoising tool emerged from the need to know whether a specific IMF contains or not useful information. Thus, significance IMF test procedures were recently developed [48] based on the statistical analysis of modes resulted from the decomposition of signals. Here, the classification of the EMD modes is based on the evaluation of the normalized Cross-Correlations at lag of zero (CC) between the signal and each Intrinsic Mode Function (IMF) and a threshold value  $CC_{TH}$  to identify statistically relevant components. In detail, the HHT decomposes the signal,  $x \equiv s_{k,z}(t)$ , into  $N$  different IMFs  $y_i$  (for  $i=1,\dots,N$ ), where  $x \cong \sum_{i=1}^N y_i$ . For the  $i$ th IMF, the cross-correlation with  $x$ ,  $\hat{R}_{x,y_i}$ , can be computed as:

$$\hat{R}_{x,y_i}[m] = \begin{cases} \sum_{n=0}^{L-m-1} x[n+m]y_i^*[n] & m > 0 \\ \hat{R}_{y_i,x}^*[-m] & m < 0 \end{cases} \quad (4)$$

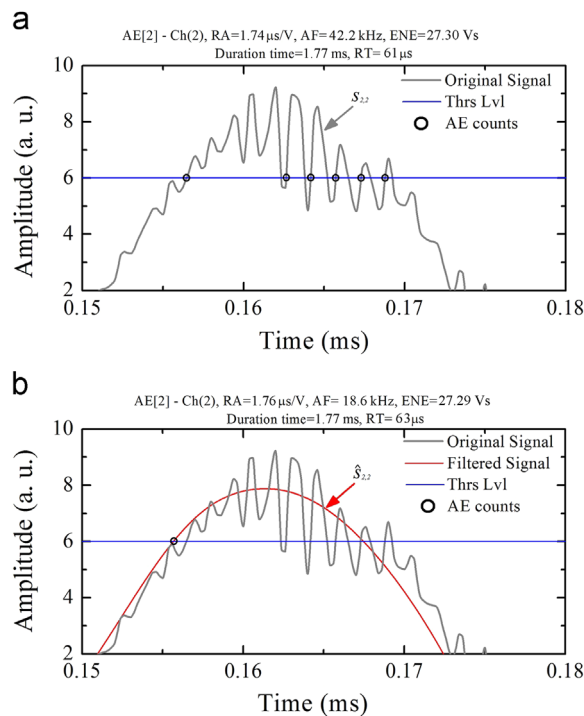


**Fig. 4.** Particular of signal dynamics showing the impact of noise filtering in the extraction of AE parameters. (a) Results obtained from original 2,2 s (gray line) and (b) from the denoised signal 2,2 s using HHT (red line). (For interpretation of the references to color, the reader is referred to the web version of this article.)

where  $y_i^*$  is the complex conjugate of  $y_i$ . The value  $CC_i = \frac{\hat{R}_{xy_i}[0]}{\|x\| \cdot \|y_i\|}$  represents the normalized cross-correlation at lag of zero ( $-1 \leq CC_i \leq 1$ ). All  $CC_i$  parameters are compared to a threshold value  $CC_{TH}$  evaluated by using Eq. (9) of Ref. [49]:

$$CC_{TH} = \frac{\max\{CC_i\}_{(i=1,\dots,N)}}{10 \times (\max\{CC_i\}_{(i=1,\dots,N)}) - 3} \quad (5)$$

All the IMFs which satisfy the condition:

$$CC_i \geq CC_{TH} \quad (6)$$

are considered to be significant for that particular signal [50].

### 3.3. Computation of AE parameters

In block (III.1) for each AE signal  $r_{k,z}(t)$ ,  $\hat{s}_{k,z}(t)$  is used to perform the quantification of AE parameters according to the procedures described in Ref. [51]. It allows to discriminate shear from the tensile cracking processes. For example, a parameter used to characterize the cracking mode is the AF, whose values are obtained from the count of AE ringdown divided by the duration time of the signal as described in Refs. [1,5]. According to this, AE parameters are evaluated in Fig. 4 demonstrating the impact of a noisy signal (AE 2, Ch.2) in the computation. An excerpt [0.15 ÷ 0.18 ms] of the entire data range ([0 ÷ 2 ms]) is represented in the figure with the aim to highlight the impact of denoising performed by HHT once is applied on the input signal  $s_{2,2}(t)$  and how the method makes recovered signal  $\hat{s}_{2,2}(t)$  retaining most of its important characters.

In Fig. 4(a) these values are determined starting from the quantification of the signal crossings (black circles) with the reference threshold (solid blue line) [27]. In the case of a noisy signal  $s_{2,2}$  (gray curve) relevant estimation errors occur. Such errors give rise to a wrong AF (42.2 kHz) computation, and might lead to inaccurate results in the damage quantification. To this aim, Fig. 4(b) depicts the denoised signal  $\hat{s}_{2,2}$ , revealing how, thanks to the drastic noise reduction provided by HHT a correct evaluation of the AF (18.6 kHz) is performed [6,17]. As consequence, all the other related parameters are evaluated more correctly.

### 3.4. Traditional time-frequency analysis

As known, high AE activity at a given area of a structure, implies the possible presence of flaw [52]. The criteria of “high” activity always need careful attention, AE hit count and rates, amplitude, and energy have formed the basis for the grading of the existing damage. The evaluation of AE hit count, AE energy, force and strain as a function of time are performed here in block (III.2) together with aggregated spectra analysis using the denoised signals  $\hat{s}_{k,z}(t)$ . Results are shown in Figs. 5–7 and discussed in Section 4.

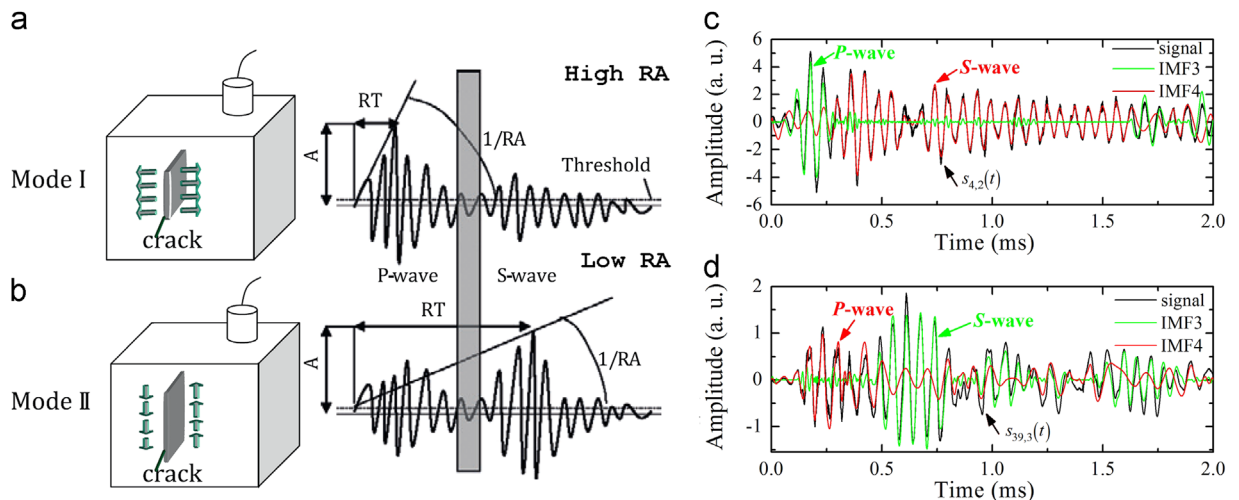


**Fig. 5.** Typical waveform attributed to (a) tensile and shear (b) fracture mode. (c) trend of the P-wave (green curve, corresponding to IMF3) and the S-wave (red curve, corresponding to IMF4) obtained by EMD in the case of compression event, and (d) trend of P-wave (red line, IMF4) and S-wave (green line, IMF3) obtained by applying EMD on a shear event. (For interpretation of the references to color in this figure legend, the reader is referred to the web version of this article.)



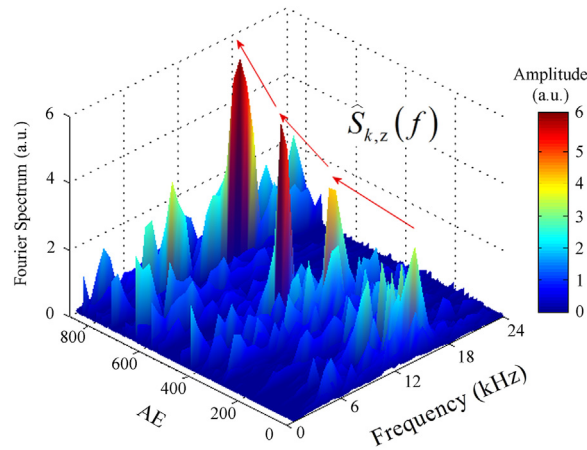


**Fig. 6.** Aggregated plot of frequency spectra for each of 879 events. (For interpretation of the references to color, the reader is referred to the web version of this article.)

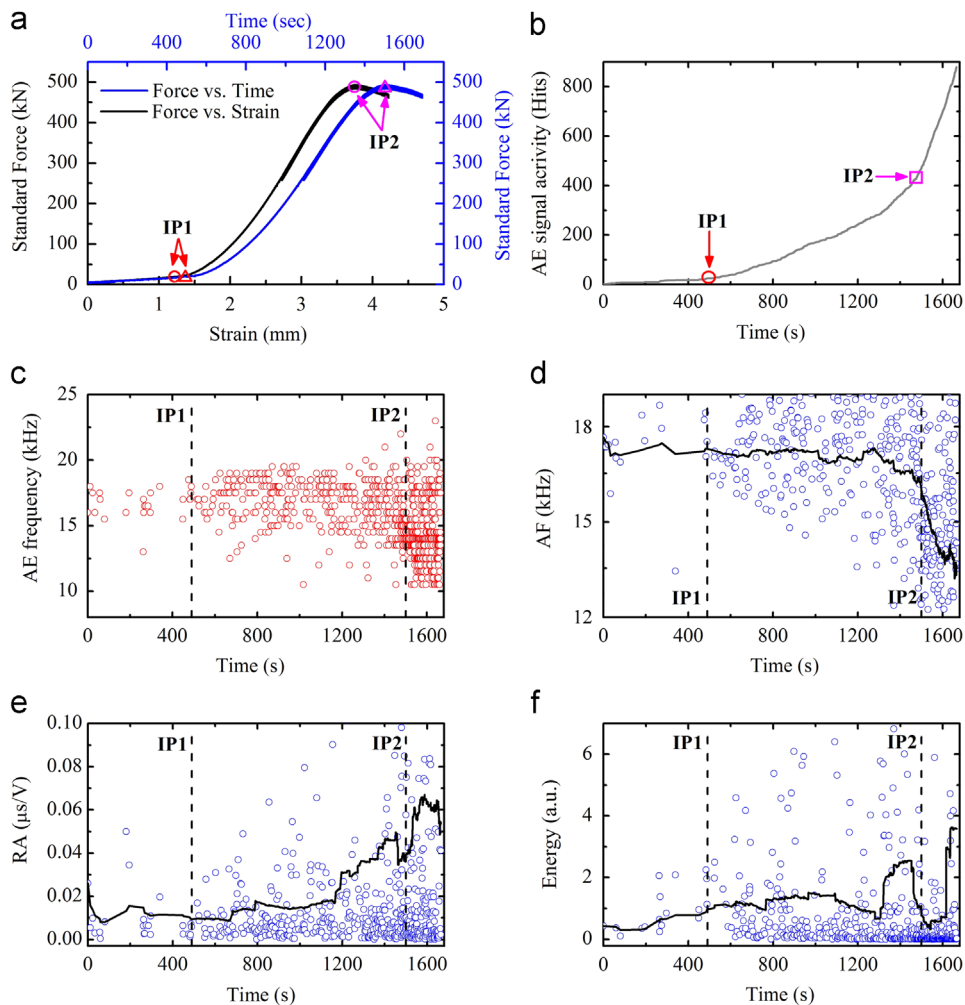


**Fig. 7.** (a) Force-vs-Time (black curve) and Force-vs-Strain (blue curve) plots with evidence of IP1 and IP2. (b) AE signal activity over time (gray curve). (c) Temporal evolution of central frequency of AE reconstructed signals  $k,z$  (red circles) and related moving average (black curve). (d) AF-vs-Time plot (blue circles) and related moving average (black curve). (e) RA-vs-Time (blue circles) and related moving average (black curve). (f) ENE-vs-Time (blue circles) and related moving average (black curve). (For interpretation of the references to color in this figure legend, the reader is referred to the web version of this article.)

### 3.5. Fracture event discrimination

The waveform of an AE signal is intrinsically representative of the underlying fracture modes related to tensile and shear deformations; therefore, the characterization of such cracking events can act as a safe measure against the final failure [4]. Basically, when a tensile event occurs, the sides of the crack move away from each other leading to a transient volumetric change in the material [41]. Therefore, most of the energy is released in the form of *P*-waves and only a small amount in the form of *S*-waves. The propagation of the former waves is faster than the latter [53]. Fig. 5(a) shows a schematic representation of an AE waveform emitted by a compression event with the propagation of *P*-waves [39], followed by *S*-waves having a smaller amplitude [54]. The corresponding RT is short [55], leading to a high RA. On the contrary, a shear cracking event (schematically represented in Fig. 5(b)) causes mainly shape deformation, which emits most of the energy in the form of *S*-waves [5,56] and only a small amount in the form of *P*-waves. Therefore, the larger amount of energy is detected after the initial onset of faster *P*-waves. In other words, the cracking event is characterized by a longer RT and then a shorter RA.

#### 3.5.1. Separation of *P*- from *S*-waves

The role of block III.3 is the analysis of the reconstructed signal and its complete IMF set to provide a robust damage classification. Thanks to the IMFs, we are able to perform a correct discrimination of which part of the AE waveform can be interpreted as *P*- or *S*-wave. The classification of the main fracture modes from IMFs is based on the evaluation of CC as already described in Section 3.2, and the Pearson Distance which measures the mutual similarity between two different IMFs.

From Eq. (5) we can determine the threshold value to extract significant IMFs from a particular AE. Only the two IMFs which, at the same time, have larger  $|CC_{y_i, y_j}|$  and satisfy the condition of Eq. (6) are used for the event type discrimination. Most of the AEs exhibit only two IMFs which satisfy Eq. (6), but when this is not the case, the absolute Pearson distance  $d_{y_i, y_j}$  ( $i < j$ ) between two IMFs is evaluated as [57]:

$$d_{y_i, y_j} = 1 - |PCC_{y_i, y_j}| = 1 - \left| \frac{1}{L-1} \sum_{k=1}^L \left( \frac{y_i[k] - \bar{y}_i}{\sigma_i} \right) \left( \frac{y_j[k] - \bar{y}_j}{\sigma_j} \right) \right| \quad (7)$$

where  $L$  is the number of elements of the IMF,  $\bar{y}_i = \frac{1}{L} \sum_{k=1}^L y_i[k]$ ,  $\sigma_i$  is the standard deviation  $\sigma_i = \sqrt{\frac{1}{L-1} \sum_{k=1}^L (y_i[k] - \bar{y}_i)^2}$  (the same applies for  $\bar{y}_j$  and  $\sigma_j$ ),  $PCC_{y_i, y_j}$  is called Pearson Product-moment correlation coefficient. The  $d_{y_i, y_j}$  is computed for all the combinations among IMFs which satisfy Eq. (6) (for instance, in the case we consider IMF3, IMF4 and IMF5, the computed Pearson Distances are  $d_{y_3, y_4}$ ,  $d_{y_3, y_5}$ , and  $d_{y_4, y_5}$ ). The values of  $d_{y_i, y_j}$  are compared to a critical value  $d_{cr}$  identified by following the Evans criterion for very weak relationships  $|PCC_{y_i, y_j}| = 0.10$  ( $d_{cr} = 0.90$ ) [58], so that:

$$d_{y_i, y_j} \geq d_{cr} \quad (8)$$

The  $y_i$  and  $y_j$  having the larger Pearson distance and that, at the same time, satisfy Eq. (8) are selected for the computational block (III.3) otherwise the AE event is not analyzed.

Previous applications of HHT in same scenario [59] have emphasized different and limited aspects of the technique [60,61]. The role of HHT in block (III.3) is to separate *P*- from *S*-wave without the user intervention. Fig. 5(c) shows the *P*-wave (green curve, corresponding to IMF3) and the *S*-wave (red curve, corresponding to IMF4) extracted from the signal as processed using HHT (black curve) of AE of event 4 (Ch.2),  $s_{4,2}(t)$ , as expected the *P*-wave moves faster and has a larger amplitude than *S*-wave. Fig. 5(d) shows the *P*-wave (red curve, corresponding to IMF4), and the *S*-wave (green curve, corresponding to IMF3) extracted from the reconstructed signal of AE event 39 (Ch.3),  $s_{39,3}(t)$  (black curve) where *P*-wave has lower intensity than *S*-wave [62].

### 3.6. AE localization

AE source localization by using an array of spatially distributed sensors has received considerable interests in recent years [63,64]. Although localization is becoming available to the general public in outdoor applications, by means of GPS receivers, event source determination in an indoor environment is still a difficult task because the TDOA is a nonlinear function of the source coordinates [65] and wave propagation speed cannot be easily calculated. For this reason, accurate 3D Localization and speed estimation based on MLT are also implemented. Traditionally, source locations are calculated by the differences in arrival times of *P*-waves at the different transducers [16,36]. A minimum number of five ( $M=5$ ) devices is necessary to determine uniquely the 3D source position and the *P*-wave propagation velocity. In [66] a solution to the corresponding system of equations is provided by an iterative algorithm and the application of a least squares approach to calculate time residuals. On the contrary, an approach which imposes the linearization of the system of equations was previously investigated in [63,67]. Taking in consideration that propagation speed is unknown [68], we adopt a joint speed and position estimation method based on TDOA which was originally developed in [69], but extended here in 3D space.

Basically, the procedure of the estimation of the crack position can be split in two main independent phases, time delay computation, and position and speed evaluations.



$\widehat{S}_{k,z}(t)$  are used as input for the MLT block (III.4) which evaluates the arrival time of the wave from all the available sensors. The algorithm uses a three-step approach where, in the first step, a least square solution introduces intermediate variables to make a linear representation of nonlinear equations and provides initial position and speed estimates.

Secondly, it refines the preliminary results by employing weighted least squares (WLS), while the last step leads to the final estimation by means of another WLS iteration [69].

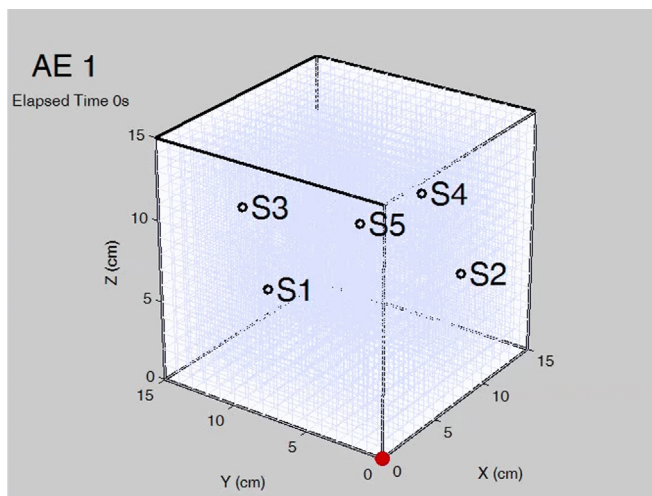
#### 4. Results

Fig. 6 displays an aggregated plot of the Fourier spectra  $|\widehat{S}_{k,z}(f)|$  of the measured AE events. For increasing AE hits, a larger amplitude (power increases from blue to red) in crack events is detected (coherently with previous observations [12,70]). The dynamical evolution of AE peak frequencies is consistent with the damage growth in cementitious structures and it has been also validated in experiments with plain and reinforced concrete [71].

The systematic evaluation of the complete set of AE parameters helps to analyze results in detail and to draw considerations related to how their values correspond or not to different cracks. Fig. 7(a) shows the force-vs-time (blue line) and force-vs-strain (black line) plots with the indication of the two IPs in the curves. The IP1 occurs at 18 kN for  $t=490$  s (red triangle) and strain  $\sigma=1.22$  mm (red circle) and can be related to the nucleation of micro-cracks, while the second one occurs at 493 kN, for  $t=1500$  s (magenta triangle) and  $\sigma=3.74$  mm (magenta circle) and is related to the formation of macro-cracks. The loading process linked to the IP2 introduces a shift in AF from larger to smaller values. After that, the peak load and the system behavior are strongly non linear (see also Fig. 1).

Indeed, it has been found that the RA increases, while the AF decreases as the damage is being accumulated. Additionally, these parameters vary significantly at the moment of the main crack formation [72,73], which indicates a change in the dominant failure mechanism from tensile type to shear type [41]. This is the reason why the AF drops to much lower values (moving average down to 27 kHz). Such behavior is similar to other types of specimen [11].

Fig. 7(b) shows the AE signal activity (hit count) as a function of time (gray curve). It describes the accumulated AE events during the test and also provides time references for the IPs (red circle and magenta square, respectively). In Fig. 7(c), the time evolution of the peak frequency (red circles) of AE reconstructed signals is presented (for each event, results of the channel with the highest SNR are shown). Starting from IP2 due to the damage level of the specimen, the number of peaks increases significantly. Fig. 7(d) displays the AF-vs-time (blue circles) and its moving average (black curve), of the recent 20 hits in order to show the trend clearly. In Fig. 7(e) a plot of RA-vs-time (blue circles) and related moving average (black curve) is provided. As shown in [11,53], the loading process involves a drop in AF from larger to smaller values after the peak load (IP2) and at larger compression loads. Therefore, a dominant presence of tensile cracks seems to follow the damage evolution until the collapse. In our data, a drastic reduction in AF is observed after IP2 (black dashed vertical line), which leads to complete failure. It is interesting to note how, at the moment of macro-cracks opening, several hits with low AF are observed, strongly decreasing the AF line. As a matter of fact, high (low) frequency oscillation waves can only propagate through small (large) inhomogeneities [73]. At the final phase, before the sample destruction, mainly low frequency waves are observed moving from tensile (Phase I) to shear-dominated (Phase II) domain. Our achievements are in qualitative agreement with previous conclusions [72]. In Fig. 7(f) the ENE-vs-time (blue circles) and related moving average (black



**Video S1.** 3D dynamical evolution of damages in the concrete specimen under test evaluated by our framework using TDOA data extracted from five transducers (S1–S5). Locations of the crack events are indicated by red circles. A video clip is available online. Supplementary material related to this article can be found online at <http://dx.doi.org/10.1016/j.ymsp.2015.12.004>.

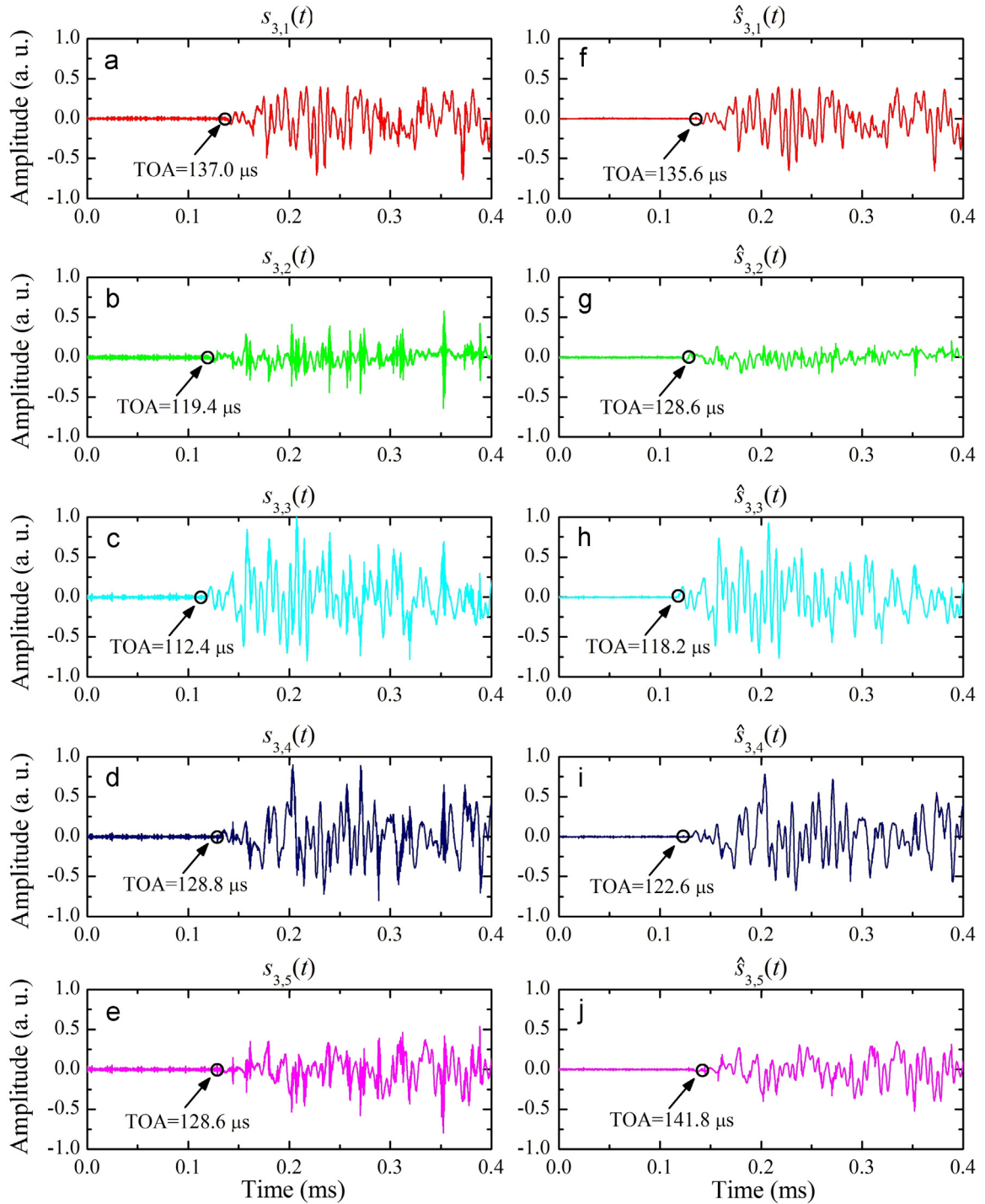


**Fig. 8.** TDOA as computed by using the signals captured from AE 1 without (a–e) and (f–l) the use of HHT. The detected Time of arrival (TOA) is indicated in each of the plots by a black circle. (For interpretation of the references to color, the reader is referred to the web version of this article.)

curve) are also displayed. The energy of the signal tends to increase during test and source fracture events. The results highlight how ENE substantially increases during the test and near the fracture the energy is 3–4 times larger than the one associated with the early damages. Again, such results are in qualitative agreement with previous findings [11].

The numerical results, taken from small geometries, enable drawing of further conclusions towards the improvement of signals classification schemes based on simple AE features. Differently from previous assumptions [74], we discover how the position of the sensors is crucial to prevent misleading results [6]. To this end, sensors must not lay on the same 2D plane,

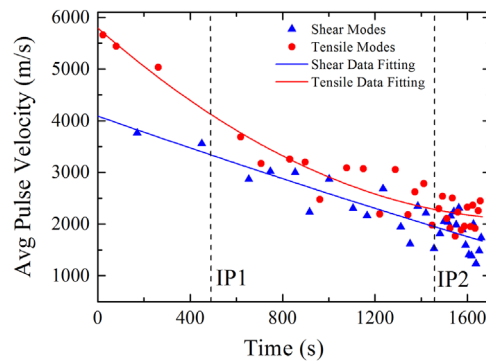


**Fig. 9.** Average pulse velocities as a function of time. (For interpretation of the references to color, the reader is referred to the web version of this article.)

this is particularly important in structures having geometrical symmetry, where sensors might be arranged along the outer surfaces and be equidistant from different points of the specimen. In such conditions, a fracture event originating, for example, along a vertical line intersecting the center of the specimen, could lead to the same TDOAs as computed from the sensors, and therefore might cause uncertainty in the source localization. A slight asymmetric arrangement of sensors, like the one proposed in Section 2, solves this problem and brings to distinct crack localization. The Supplementary Video S1, provided as additional material, shows the results of the algorithm, while the location of the crack events is indicated by a red circle.

Our experimental data highlight that compression tests in cubic specimens are ruled by a known damage mechanism. Basically, when the concrete is subject to axial compression, it expands laterally. Moreover, there are friction forces between the sample surfaces and the hydraulic press plate that cause a confinement action that contrasts with the expansion operating on these surfaces. As highlighted in [75], the increase of the tensile stresses provokes inclined micro-cracks on the concrete cube samples that merge near the corners with a bipyramidal mechanism, so the cracks are concentrated in the surfaces and on its edges. In particular, the crack evolution shows a pattern underlined in [76] in which lateral sides of the samples get spalled and there is a dense columnar cracking in the bulk of the specimens. The impact of HHT in TDOA computation and therefore in crack evolution is discussed in Fig. 8. TDOAs are extracted from the processed AE event signals  $\widehat{s}_{k,z}(t)$  according to Ref. [77] whereas a comparison is represented between such parameters as estimated from AE 1 data without (a–e) and with (f–i) the use of HHT. We point out how the computation of the spatial distribution of the cracks in the sample using TDOA achieved without HHT denoising gives rise to a non bipyramidal fracture which is inconsistent with both the operator observation during the measurements and the data presented in literature [78]. Thanks to the HHT, we are able not only to identify the onset of a propagating event from measured signals, but to also discriminate the arrival time of the *P*-wave and the *S*-wave, evaluating, if necessary, the average propagating speed for tensile and shear events (in block III.4) [79]. Our computations reveal how the wave speed related to the energy release at the later levels of damage (mix-mode cracks) is always slower than the earlier levels of damage (pure flexural cracks), as shown in Fig. 9. This fact can be explained by the large part of energy that is transferred in the form of shear mode.

We find that, during the compression test, the ratio between the tensile and shear velocity decreases. This can be related to the damages in the microstructure of the specimen that reduce its elastic characteristics [80]. In fact, in [81] the damage index is evaluated by using the ratio between the tensile and shear wave velocity in a compression test. Such index decreases with the increase of the damage in the sample. Moreover, the maximum peak of the waveform delays considerably when compared to the onset of the initial longitudinal arrivals [70].

The analysis of the energy content obtained from AE signals (Fig. 7(f)), enables to state how, also in this case the damage evolution leads to stronger signals after the peak load. For increasing AE hits, larger amplitude failure events are detected into the concrete samples. Therefore, such diverse dominant fracture modes can be accurately classified using our framework.

## 5. Discussion

The results have highlighted that AEs data during the early damage stage (corresponding to tensile mode) exhibit large AF and lower RA, while, as the material is driven to final failure, AF decreases and RA increases. MLT provides an adaptive method to evaluate the 3D positioning of cracks and their time evolution on concrete structures under test. By localizing AE sources, damage or material flaws can be finally detected.

If AE source characteristics have to be analyzed quantitatively in order to investigate damage mechanisms, the knowledge of the damage locations is a primary requirement [82].

To this end, our findings are in strict agreement with theoretical predictions [13] and suggest how the HHT, in particular, can be a valuable tool in the investigation of AE events and it can lead to the development of a systematic and unsupervised

processing framework, where both a well-defined classification of the stress types and accurate assessment of the structural health status can be achieved. Under the loading tests, AE parameters are extracted: traditional time (e.g. hit accumulation) and frequency analysis are used to evaluate damage and spectral information during time, while event-type discrimination is performed leveraging on the distinguished *P* and *S*-wave contributions. During crack growth, experimental findings suggest how damage originates from the top of the surface and progressively propagates in the structure until the final collapse.

## 6. Conclusions

To obtain information on the damage evolution in materials and structures, a pivotal signal processing framework has been developed to enhance the characterization of failure mechanisms and provide advanced tools for robust and systematic AE analysis. To this end, we have extended and combined complementary techniques to optimize classification of cracking modes.

Firstly, a TFR is used to correct the impact of transducer frequency response in measurements. Secondly, the HHT, as an advanced nonlinear and nonstationary technique, is used to exploit its well-known systematic filtering and modal discrimination features. To date, systematic procedures for the enhancement and the full processing of AE signals do not exist. Therefore, the results can be hardly compared or transposed among different SHM systems. First of all, the HHT provides a superior well known denoising performance if compared with traditional filtering methods [36] that can help in getting more realistic information from AE parameters. In addition, the HHT permits to carefully discriminate and analyze both *P*- and *S*- components in propagating waves enabling a robust and unsupervised characterization of the AE type. In other words, the advantage of both adaptive denoising capabilities of HHT and modal separation (EMD) features permit to isolate and investigate independent transient stress waves (*P*- and *S*-), including their amplitude, with the evident advantage to extract more information and details on the nature of the AE in a systematic way.

Thirdly, while many TDOA based methods [83–85] assume that the propagation speed is known, here both target position and propagation speed are estimated jointly also considering that the wave velocity changes as a function of the number of AEs.

In conclusion, the techniques in the proposed framework can be considered highly competitive descriptors of the damage potential of a concrete structure and aid more in-depth analysis performed by domain experts. In addition, the methods presented here provide promising capabilities for real time monitoring in large scale applications.

## Acknowledgments

This work has been supported by the following projects: PRIN2010ECA8P3 and PON04a2\_F named SIGLOD, both funded by the Italian MIUR. The authors thank Domenico Romolo for making the graphical abstract.

## References

- [1] A. Carpinteri, M. Corrado, G. Lacidogna, "Heterogeneous materials in compression: Correlations between absorbed, released and acoustic emission energies", *Eng. Fail. Anal.* 33 (2013) 236–250.
- [2] G. Lacidogna F. Accornero M. Corrado A. Carpinteri, Crushing and fracture energies in concrete specimens monitored by acoustic emission, In: Proceedings of the VIII International Conference on Fracture Mechanics of Concrete and Concrete Structures, FraMCoS-8, 2013.
- [3] F. Lamonaca, D. Grimaldi, Trigger realignment by networking synchronized embedded hardware, *IEEE Trans. Instrum. Meas.* 62 (2) (2013) 38–49.
- [4] D.G. Aggelis, T. Shiotani, A. Papacharalampopoulos, D. Polyzos, The influence of propagation path on elastic waves as measured by acoustic emission parameters, *Struct. Health Monit.* 11 (3) (2011) 359–366.
- [5] E. Di Battista, Acoustic emission and fracture energy dissipation in notched concrete beams subjected to three-point bending tests, XXI Convegno dell'Associazione Italiana di Meccanica Teorica ed Applicata, Turin, Italy, 17–20 Sep., 2013.
- [6] D.G. Aggelis, A.C. Mpalaskas, D. Ntalakas, T.E. Matikas, Effect of wave distortion on acoustic emission characterization of cementitious materials, *Constr. Build. Mater.* 35 (2012) 183–190.
- [7] M. Ohtsu, Acoustic Emission (AE) and Related Non-destructive Evaluation (NDE) Techniques in the Fracture Mechanics of Concrete, Woodhead Publishing, United Kingdom, ISBN 978-1-78242-327-0, 2015.
- [8] A. Carpinteri, G. Lacidogna, F. Accornero, A.C. Mpalaskas, T.E. Matikas, D.G. Aggelis, Influence of damage in the acoustic emission parameters, *Cem. Concr. Compos.* 44 (2013) 9–16.
- [9] E. Dehghan Niri, A. Farhizadeh, S. Salamone, Determination of the probability zone for acoustic emission source location in cylindrical shell structures, *Mech. Syst. Signal Process.* 60–61 (2015) 971–985.
- [10] D.D. Doan, E. Ramasso, V. Placet, S. Zhang, L. Boubakar, N. Zerhouni, An unsupervised pattern recognition approach for AE data originating from fatigue tests on polymer–composite materials, *Mech. Syst. Signal Process.* 64–65 (2015) 465–478.
- [11] D.G. Aggelis, Classification of cracking mode in concrete by acoustic emission parameters, *Mech. Res. Commun.* 38 (2011) 153–157.
- [12] D.G. Aggelis, T. Shiotani, S. Momoki, A. Hirama, Acoustic emission and ultrasound for damage characterization of concrete elements, *ACI Mater. J.* 106 (6) (2009) 509–514.
- [13] V.M. Malhotra, Testing Hardened Concrete: Non-Destructive Methods Monograph 9, American Concrete Institute, Detroit, 1976.
- [14] T. Suzuki, H. Ogata, R. Takada, M. Aoki, M. Ohtsu, Use of acoustic emission and X-ray computed tomography for damage evaluation of freeze-thawed concrete, *Constr. Build. Mater.* 24 (12) (2010) 2347–2352.
- [15] P. Rossi, J.L. Tailhan, F. Le Maou, L. Gaillet, E. Martin, Basic creep behavior of concretes investigation of the physical mechanisms by using acoustic emission, *Cem. Concr. Res.* 42 (2012) 61–73.



- [16] C.U. Grosse, M. Ohtsu, *Acoustic Emission Testing* ISBN 978-3-540-69895-1, Publisher Springer, Heidelberg, 2008.
- [17] D.G. Aggelis, A.C. Mpalaskas, T.E. Matikas, Investigation of different fracture modes in cement-based materials by acoustic emission, *Cem. Concr. Res.* 48 (2013) 1–8.
- [18] J.H. Bungey, S.G. Millard, M.G. Grantham, *Testing of Concrete in Structures*, 4th ed, Publisher Taylor and Francis, New York, USA, 2008, ISBN10: 0-415-26301-8.
- [19] E. Maillet, G.N. Morscher, Waveform-based selection of acoustic emission events generated by damage in composite materials, *Mech. Syst. Signal Process.* 52–53 (2015) 217–227.
- [20] N.E. Huang, Z. Shen, S.R. Long, M.C. Wu, H.H. Shih, Q. Zheng, N.C. Yen, C.C. Tung, H.H. Liu, The empirical mode decomposition and the Hilbert spectrum for nonlinear and non-stationary time series analysis, *Proc. R. Soc.* 454 (1998) 903–995.
- [21] N.E. Huang, Z. Shen, S.R. Long, A new view of nonlinear water waves: the Hilbert spectrum, *Annu. Rev. Fluid Mech.* 31 (1999) 417–457.
- [22] E. Tsangouri, D.G. Aggelis, K. Van Tittelboom, N. De Belie, D. Van Hemelrijck, Detecting the activation of a self-healing mechanism in concrete by acoustic emission and digital image correlation, *Sci. World J.* 2013 (2013) 10. Article ID 424560.
- [23] G. Siracusano, A. La Corte, A comparison between advanced time-frequency analyses of non-stationary magnetization dynamics in spin-torque oscillators, *Physica B* 435 (2014) 66–70.
- [24] G. Consolo, G. Finocchio, G. Siracusano, S. Bonetti, A. Eklund, J. Åkerman, B. Azzerboni, Non-stationary excitation of two localized spin-wave modes in a nano-contact spin torque oscillator, *J. Appl. Phys.* 114 (15) (2013) 153906.
- [25] G. Siracusano, A. La Corte, V. Puliafito, G. Finocchio, A generalized tool for accurate time-domain separation of excited modes in spin-torque oscillators, *J. Appl. Phys.* 115 (2014) 17D108.
- [26] D. Muñoz, F. Bouchereau, C. Vargas, R. Enríquez-Caldera, *Position Location Techniques and Applications*, Elsevier Publisher, Burlington, MA 01803, USA, ISBN 978-0-12-374353-4, 2009.
- [27] F. Lamonaca, A. Carrozzini, D. Grimaldi, R.S. Olivito, Improved monitoring of acoustic emissions in concrete structures by multi-triggering and adaptive acquisition time interval, *Measurement* 59 (2015) 227–236.
- [28] A. Carpinteri, G. Lacidogna, G. Niccolini, S. Puzzi, Critical defect size distributions in concrete structures detected by the acoustic emission technique, *Meccanica* 43 (2008) 349–363.
- [29] M. Ohtsu, Recommendations of RILEM Technical Committee 212-ACD: acoustic emission and related NDE techniques for crack detection and damage evaluation in concrete, *Mater. Struct.* 43 (9) (2010) 1177–1189.
- [30] F. Lamonaca, A. Carrozzini, Monitoring of acoustic emissions in civil engineering structures by using time frequency representation, *Sensors Transducers J.* 8 (2010) 42–53.
- [31] M.R. Kaphle, A.C.C. Tan, D.P. Thambiratnam, T.H.T. Chan, Study of acoustic emission data analysis tools for structural health monitoring applications, in: *Progress in Acoustic Emission XV: Proceedings of the 20th International Acoustic Emission Symposium*, Japanese Society for Non-Destructive Inspection Kumamoto, Japan, 2010, pp. 1–6.
- [32] BS EN 12390-3:2002, Testing hardened concrete. Compressive strength of test specimens, ed: CEN – European Committee for Standardization, 2003.
- [33] F. Garesci, S. Flieger, Young's modulus prediction of long fiber reinforced thermoplastics, *Compos. Sci. Technol.* 85 (2013) 142–147.
- [34] F. Garesci, Static and dynamic analysis of bonded sandwich plates, *Int. J. Adhes. Adhes.* 33 (2012) 7–14.
- [35] F. Lamonaca, D.L. Carni, A. Carrozzini, D. Grimaldi, R.S. Olivito, Mul ti-triggering and signal extraction for acoustic emissions monitoring, in: *Proceedings of Metrology for Aerospace (MetroAeroSpace) IEEE*, 2014, pp. 383–387, doi: 10.1109/MetroAeroSpace.2014.6865954.
- [36] A. Carpinteri, G. Lacidogna, *Acoustic Emission and Critical Phenomena*, Taylor & Francis Group, London, UK, ISBN 978-0-203-89222-0, 2008.
- [37] BS EN 13477-2:2001, Non-destructive testing. Acoustic emission. Equipment characterization. Verification of Operating Characteristics, 2001.
- [38] S. Colombo, M.C. Forde, I.G. Main, M. Shigeishi, Predicting the ultimate bending capacity of concrete beams from the 'Relaxation Ratio' analysis of AE signals, *Constr. Build. Mater.* 19 (2005) 746–754.
- [39] D.G. Aggelis, T.E. Matikas, Effect of plate wave dispersion on the acoustic emission parameters in metals, *Comput. Struct.* 98–99 (2012) 17–22.
- [40] M. Ohtsu, M. Uchida, T. Okamoto, S. Yuyama, Damage assessment of reinforced concrete beams qualified by acoustic emission, *ACI Struct. J.* 99 (4) (2002) 411–417.
- [41] D.G. Aggelis, D.V. Soulioti, N. Sapouridis, N.M. Barkoula, A.S. Paipetis, T.E. Matikas, Acoustic emission characterization of the fracture process in fibre reinforced concrete, *Constr. Build. Mater.* 25 (2011) 4126–4131.
- [42] X. Xiong, S. Yang, C. Gan, A new procedure for extracting fault feature of multi-frequency signal from rotating machinery, *Mech. Syst. Signal Process.* 32 (2012) 306–319.
- [43] L. Calabrese, G. Campanella, E. Proverbio, Noise removal by cluster analysis after long time AE corrosion monitoring of steel reinforcement in concrete, *Constr. Build. Mater.* 34 (2012) 362–371.
- [44] D.D. Doan, E. Ramasso, V. Placet, S. Zhang, L. Boubakar, N. Zerhouni, An unsupervised pattern recognition approach for AE data originating from fatigue tests on polymer-composite materials, *Mech. Syst. Signal Process.* 64–65 (2015) 465–478.
- [45] D. Bianchi, E. Mayrhofer, M. Gröschl, G. Betz, A. Vernes, Wavelet packet transform for detection of single events in acoustic emission signals, *Mech. Syst. Signal Process.* 64–65 (2015) 441–451.
- [46] M.E. Zitto, R. Piotrkowski, A. Gallego, F. Sagasta, A. Benavent-Climent, Damage assessed by wavelet scale bands and *b*-value in dynamical tests of a reinforced concrete slab monitored with acoustic emission, *Mech. Syst. Signal Process.* 60–61 (2015) 75–89.
- [47] Z. Zhang, Y. Leng, Y.K. Yang, X. Xiao, S. Ge, Comparative study on wavelet coherence and HHT coherence, 7th Int. Congr. Image Signal Process. (CISP 2014), 2014, pp. 867–872.
- [48] P. Flandrin, G. Rilling, P. Gonçalvès, Empirical mode decomposition as a filter bank, *IEEE Signal Process. Lett.* 11 (2004) 112–114.
- [49] A. Ayenu-Prah, N. Attoh-Okin, A criterion for selecting relevant intrinsic mode functions in empirical mode decomposition, *Adv. Adapt. Data Anal.* 2 (1) (2010) 1–24.
- [50] N.E. Huang, Z. Wu, Statistical Significance Test of Intrinsic Mode Functions, (in N. E. Huang and S. Shen, Hilbert–Huang Transform and its Applications), first edition, . World Scientific Publishing Company, Singapore, 2005.
- [51] K. Ohno, M. Ohtsu, Crack classification in concrete based on acoustic emission, *Constr. Build. Mater.* 24 (12) (2010) 2339–2346.
- [52] K. Ono, Structural integrity evaluation using acoustic emission, *J. Acoust. Emiss.* 25 (2007) 1–20.
- [53] D.G. Aggelis, T.E. Matikas, T. Shiotani, Advanced acoustic techniques for health monitoring of concrete structures, in: S.H. Kim, K.Y. Ann (Eds.), *The Song's Handbook of Concrete Durability*, Middleton Publishing Inc, Seoul, Korea, 2010, pp. 331–378.
- [54] C.U. Grosse, F. Finck, Quantitative evaluation of fracture processes in concrete using signal-based acoustic emission techniques, *Cem. Concr. Compos.* 28 (4) (2006) 330–336.
- [55] D. Soulioti, N.M. Barkoula, A. Paipetis, T.E. Matikas, T. Shiotani, D.G. Aggelis, Acoustic Emission behavior of steel fibre reinforced concrete under bending, *Constr. Build. Mater.* 23 (2009) 3532–3536.
- [56] C.U. Grosse, F. Finck, J.H. Kurz, H.W. Reinhardt, Improvements of AE technique using wavelet algorithms, coherence functions and automatic data analysis, *Constr. Build. Mater.* 18 (2004) 203–213.
- [57] M.H. Fulekar, *Bioinformatics: Applications in Life and Environmental Sciences*, Springer Publisher, New Delhi, India, ISBN 1-4020-8879-5, 2009.
- [58] J.D. Evans, *Straightforward Statistics for the Behavioral Sciences*, Brooks/Cole Publishing, Pacific Grove, California, 1996.
- [59] S.S. Law, X.Q. Zhu, Damage assessment of reinforced concrete using Hilbert–Huang transform. Conference: 2005 IMAC-XXIII: Conference & Exposition on Structural Dynamics, The Hong Kong Polytechnic University, 2005, pp. 1–6.
- [60] F.X. Ye, X.X. Zha, H.X. Wang, The application of a HHT based ultrasonic detecting method in quality assessment of CSFT, *Adv. Steel Constr.* 7 (2) (2011) 182–191.



- [61] A. Gu, Y. Luo, B. Xu, Characteristic identification of cracking acoustic emission signals in concrete beam based on Hilbert–Huang transform, *Advances in Acoustic Emission Technology: Proceedings of the World Conference on Acoustic Emission – 2013*, Springer Proceedings in Physics, Vol. 158, 2015, pp. 205–216, doi: 10.1007/978-1-4939-1239-1\_19.
- [62] G. Finocchio, O. Casablanca, G. Ricciardi, U. Alibrandi, F. Garesci, M. Chiappini, B. Azzerboni, *Appl. Phys. Lett.* 104 (2014) 191903.
- [63] L.J. Dong, X.B. Li, G. Xie, An analytical solution for acoustic emission source location for known P wave velocity system, *Math. Prob. Eng.* 2014 (2014) 6. Article ID 290686.
- [64] P. Sedlak, Y. Hirose, M. Enoki, Acoustic emission localization in thin multi-layer plates using first-arrival determination, *Mech. Syst. Signal Process.* 36 (2013) 636–649.
- [65] R. Zhang, F. Höflinger, L. Reindl, TDOA-based localization using interacting multiple model estimator and ultrasonic transmitter/receiver, *IEEE T Instrum. Meas.* 62 (8) (2013) 2205–2214.
- [66] A. Carpinteri, G. Lacidogna, G. Niccolini, Critical behaviour in concrete structures and damage localization by acoustic emission, *Key Eng. Mater.* 312 (2006) 305–310.
- [67] R. Bucher, D. Misra, A synthesizable VHDL model of the exact solution for three-dimensional hyperbolic positioning system, *VLSI Des.* 15 (2) (2002) 507–520.
- [68] E.K. Skarsoulis, G.S. Piperakis, Use of acoustic navigation signals for simultaneous localization and sound-speed estimation, *J. Acoust. Soc. Am.* 125 (2) (2009) 1384–1393.
- [69] J. Zheng, K.W.K. Lui, H.C. So, Accurate three-step algorithm for joint source position and propagation speed estimation, *Signal Process.* 87 (2007) 3096–3100.
- [70] M.A.A. Aldahdooh, N.M. Bunnori, M.A.M. Johari, Damage evaluation of reinforced concrete beams with varying thickness using the acoustic emission technique, *Constr. Build. Mater.* 44 (2013) 812–821.
- [71] J.H. Kurz, F. Finck, C.U. Grosse, H.W. Reinhardt, Stress drop and stress redistribution in concrete quantified over time by the *b*-value analysis, *Struct. Health Monit.* 5 (2005) 69–81.
- [72] S. Kabir, P. Rivard, D.C. He, P. Thivierge, Damage assessment for concrete structure using image processing techniques on acoustic borehole imagery, *Constr. Build. Mater.* 23 (10) (2009) 3166–3174.
- [73] E.N. Landis, S.P. Shah, Frequency-dependent stress wave attenuation in cement-based materials, *J. Eng. Mech.* 121 (1995) 737–743.
- [74] F. Lamonaca, A. Carrozzini, D. Grimaldi, R.S. Olivito, Acoustic emission monitoring of damage concrete structures by multi-triggered acquisition system, in: *Proceedings of IEEE International Instrumentation and Measurement Technology Conference (I2MTC)*, 13–16 May, 2012, pp. 1630–1634, doi: 10.1109/I2MTC.2012.6229657.
- [75] Z.P. Bazant, X.J. Xiang, Size effect in compression fracture: splitting crack band propagation, *J. Eng. Mech.* 123 (2) (1997) 162–172.
- [76] J.R. del Viso, J.R. Carmona, G. Ruiz, Shape and size effects on the compressive strength of high-strength concrete, *Cem. Concr. Res.* 38 (3) (2008) 386–395.
- [77] B. Babjak, S. Szilvasi, P. Volgyesi, O. Yapar, Analysis and efficient onset time detection of acoustic emission signals with power constrained sensor platforms, *Sensors* 2013 (2013) 1–4.
- [78] M.B. Norazura, R. Pullin, K.M. Holford, R.J. Lark, A practical investigation into acoustic wave propagation in concrete structures, *Adv. Mater. Res.* 13–14 (2006) 205–212.
- [79] P. Annibale, R. Rabenstein, Sound speed estimation from time of arrivals-derivation and comparison with TDOA-based estimation, In: *Proceedings of 20th European Signal Processing Conference (EUSIPCO)*, 27–31 Aug. 2012, pp. 1014–1018.
- [80] P. Rossi, N. Godart, J.L. Robert, J.P. Gervais, D. Bruhat, Investigation of the basic creep of concrete by acoustic emission, *Mater. Struct.* 27 (1994) 510–514.
- [81] F. Pellet, G. Fabre, Damage evaluation with P-wave velocity measurements during uniaxial compression tests on argillaceous rocks, *Int. J. Geomech.* 7 (6) (2007) 431–436.
- [82] Y. Xu, D. Xu, J. Qu, X. Cheng, H. Jiao, S. Huang, Concrete crack damage location based on piezoelectric composite acoustic emission sensor, *Advances in Acoustic Emission Technology*, in: Shen Gongtian, Wu Zhanwen, Zhang Junjiao (Eds.), Springer Proceedings in Physics, 158, 2015, pp. 347–353.
- [83] S. Gezici, T. Zhi, G.B. Giannakis, H. Kobayashi, A.F. Molisch, H.V. Poor, Z. Sahinoglu, Localization via ultra-wideband radios: a look at positioning aspects for future sensor networks, *IEEE Signal Process. Mag.* 22 (4) (2005) 70–84.
- [84] A. Mahajan, M. Walworth, 3-D position sensing using the differences in the time of-flights from a wave source to various receivers, *IEEE Trans. Robot. Autom.* 17 (2001) 91–94.
- [85] P. Stoica, J. Li, Lecture notes-source localization from range-difference measurements, *IEEE Signal Process. Mag.* 23 (6) (2006) 63–66.